Composite Structures 136 (2016) 358–371

Contents lists available at ScienceDirect

Composite Structures

journal homepage: www.elsevier.com/locate/compstruct

Dissipative elastic metamaterials for broadband wave mitigation at subwavelength scale

Y.Y. Chen [a], M.V. Barnhart [a], J.K. Chen [a], G.K. Hu [b], C.T. Sun [c], G.L. Huang [a,*]

[a] Department of Mechanical and Aerospace Engineering, University of Missouri, Columbia, MO 65211, USA
[b] School of Aerospace Engineering, Beijing Institute of Technology, Beijing 100081, China
[c] School of Aeronautics and Astronautics, Purdue University, West Lafayette, IN 47907, USA

ARTICLE INFO

Article history:

Keywords:
Microstructure design
Broadband wave mitigation
Dissipative elastic metamaterials

ABSTRACT

In this paper, an elastic metamaterial with multiple dissipative resonators is presented for broadband wave mitigation by properly utilizing interactions from resonant motions and viscoelastic effects of the constitutive material. The working mechanism of the metamaterial to suppress broadband waves is clearly revealed in a dissipative mass-in-mass lattice system through both negative effective mass density and effective metadamping coefficient. Based on the novel metadamping mechanism, a microstructure design of the dissipative metamaterial made of multi-layered viscoelastic continuum media is first proposed for efficient attenuation of a transient blast wave. It is found that the extremely broadband waves can be almost completely mitigated with metamaterials at subwavelength scale. The results of the study could be used in developing new multifunctional composite materials to suppress the shock or blast waves which may cause severe local damage to engineering structures.

1. Introduction

Metamaterials are engineered structural materials that possess unique dynamic effective properties, not commonly found in nature. In recent years, a great deal of theoretical, numerical and experimental research has been conducted on electromagnetic metamaterials with novel applications such as electromagnetic absorbers, negative refractive indices, cloaking and superlensing [1–3]. Because of the analogy between electromagnetic waves and acoustic waves, acoustic metamaterials hold the potential to perform similar novel functions with acoustic waves as those found in electromagnetic metamaterials [4–9]. The key idea and principal component in microstructure design of acoustic metamaterials is to introduce subwavelength locally resonant inclusions, or, resonators. Due to the subwavelength feature, acoustic metamaterials can be modeled as effective continuum media with frequency dependent effective mass densities and/or bulk moduli.

The realm of elastic metamaterial research is a relatively new field that also presents exciting and novel applications related to manipulation of elastic (longitudinal and transverse) waves and plate guided waves. The label Elastic MetaMaterials (EMMs) refers to a class of periodic structural materials, consisting of a solid-phase host and arrays of internal resonators, which are capable of affecting the propagation of elastic waves. For most configurations, the resonators typically consist of structural elements with highly contrasting elastic properties. For example, the very first EMM archetype was realized by embedding rubber-coated lead spheres in an epoxy matrix to capture dipolar resonances [10]; an anomalous bandgap (400–600 Hz) was observed with this architecture even for small spherical inclusions (5 mm radius) at subwavelength scale. By using a mass-in-mass lattice system to represent an EMM, it was found that the negative effective mass density could be achieved and this phenomena has been experimentally realized in a relatively low-frequency domain [11,12], which results in the prohibition of low-frequency wave propagation across the metamaterial at subwavelength scale. Unfortunately, EMM configurations involving geometrically simple resonators have limited applicability, as they offer limited design opportunities to tune (widen and/or shift) the bandgaps – a problem that has been only partially alleviated using geometry or topology optimization. For example, it has been shown that, by embedding multiple heavy inclusions into a rubber matrix, an EMM can engage monopolar, dipolar and quadrupolar resonances associated with different dynamics of the resonating masses [13]. As a result, the EMM can simultaneously feature negative effective mass density and negative effective elastic moduli. Recently, a new chiral EMM configuration consisting of a three-phase or

* Corresponding author.
E-mail address: huangg@missouri.edu (G.L. Huang).

http://dx.doi.org/10.1016/j.compstruct.2015.09.048
0263-8223/

single-phase material and capable of experiencing both dipolar and rotational microstructural resonances has been developed [14,15]. The EMM was found to simultaneously exhibit negative effective mass density and bulk modulus in a selected frequency band numerically and experimentally. However, for the designs of existing micro-inclusions or resonators, the resulting bandgaps are still relatively narrow near the locally resonant frequency, which is a fundamental challenge for practical engineering applications and further development of the EMM. In order to improve the functionality of the EMM for wave interference at broadband frequencies, there is a compelling need for a new microstructure design and wave absorption concept.

It is well known that the attenuation bandwidth can be extended through the use of multiple resonators, for which the internal resonances may be tailored to cover a range of frequencies that extends beyond that achievable with one resonator. As a first effort in exploring the problem, a metamaterial consisting of two resonators was suggested and investigated for the demonstration of multiple bandgap generation [16], which means that the elastic wave in those frequency regimes cannot propagate and wave energy is reflected back or temporarily stored in resonators. A similar metamaterial with two embedded resonators was then adopted to explore the possibility for blast wave blocking and mitigation [17]. The transient waves in those bandgap frequency regimes were efficiently mitigated by increasing the number of unit cells. Zhu et al. [18] investigated the vibration suppression abilities of a chiral EMM with multiple resonators, both analytically and experimentally to produce complete broadband vibration suppression or blocking by utilizing their individual bandgaps through a section-distributed design of multiple local resonators. It should be mentioned that, for those EMMs, the elastic wave energy is actually reflected back or blocked by the EMMs and elastic waves are not dissipated or absorbed at all because damping properties in the constituent materials are not considered in those microstructure designs.

Damping is an intrinsic property of materials and its characterization represents the degree of energy dissipation or absorption at different dynamic states. In wave mitigation applications of the resonator-based EMMs, dissipation or damping is not desired because damping will reduce the resonant motion and therefore, their ability to efficiently suppress or mitigate waves will also be reduced. A key trade-off in the broadband wave mitigation applications is that an increase in the intensity of damping commonly reduces relative motions of the resonators, or mechanical resistance capacity. The two underlying design features for the microstructure design are (1) the presence of locally resonant elements and (2) the presence of at least one constituent material phase or component that exhibits damping. Proper combination of these two features may lead to broadband wave attenuation or absorption. Inspired by the concept, Hussein and Frazier [19] and Manimala and Sun [20] studied wave propagation in the mass-in-mass lattice model by introducing damping coefficient into the single resonator. It was found that the damping can actually broaden the wave attenuation frequency regime through the analysis of wave transmission or effective high damping ratio so called "metadamping". A dissipative mechanism in two resonators was also utilized as a broadband vibration absorber for a metamaterial beam [21]. Numerical simulations in the structural level showed that for a vibration with a frequency in one of the two stopbands, the resonators are excited to vibrate in their optical modes for vibration attenuation, however, for a vibration with a frequency outside of but between the two stopbands, it can be efficiently damped out by using the damper with the second mass. However, to fully implement this concept in the material level, a comprehensive study of the dissipative EMM is highly needed to answer following fundamental questions such as: (1) how to design the microstructure of the EMM to possess the multiple bandgaps which are close to each other? (2) how to utilize the coupling of resonant motion and damping coefficients to achieve metadamping properties and form a complete broadband wave mitigation regime? (3) what is the wave attenuation ability of the proposed dissipative EMM under a transient wave loading?

In this paper, a systematic study of an EMM with multiple dissipative resonators is provided for broadband longitudinal wave mitigation by properly modeling and analyzing viscous effects of constitutive materials. Wave dispersion behavior of a non-dissipative lattice system with multiple resonators is first studied to quantitatively determine microstructure properties required to produce multiple bandgaps. Then, wave propagation of a dissipative lattice system with multiple resonators is investigated. Attention is focused on achieving a wide wave attenuation band through properly selecting the damping coefficients in the each of the constitutive elements. To reveal the working mechanisms, the dissipative EMM is homogenized as an effective medium with an effective mass and an effective metadamping coefficient, from which wave attenuation can be quantitatively interpreted by the negative effective mass density and effective metadamping. For one example of an engineering application, a transient analysis of the proposed lattice system with finite unit cells is performed to demonstrate and validate the efficiency and ability to mitigate a blast wave. Finally, a microstructure design of the dissipative EMM made of the heterogeneous continuum media with damping coefficients included in the constitutive materials is numerically proposed as a potential EMM candidate for broadband wave mitigation. Hopefully, the results of the study can open new opportunities in the development of a new multifunctional composite as efficient wave mitigation materials to suppress the broadband shock or blast waves.

2. Non-dissipative mass-in-mass lattice system with multiple resonators

2.1. Wave dispersion of the non-dissipative lattice system

Bandgap structure behaviors of a multiresonator mass-in-mass lattice system were studied and investigated by Huang and Sun [16]. In the study, to further understand the underlying mechanism for the wave attenuation behavior, wave propagation in the one-dimensional (1D) lattice system is briefly iterated and revisited. As shown in Fig. 1, each unit cell contains two local resonators and is separated from each of its adjacent cells by a length, L. The three rigid masses that make up each of the unit cells are m_1, m_2, and m_3, respectively. Each of the unit cells are connected by a spring element with coefficient k_1. While the coefficient, k_2, represents the spring element between the middle mass and the outer mass and the coefficient, k_3, represents the spring element between the innermost mass and the middle mass in each unit cells.

For this two-resonator structure, equations of motion for the jth unit cell can be expressed as

$$m_1\frac{d^2u_1^{(j)}}{dt^2}+k_1\left[2u_1^{(j)}-u_1^{(j-1)}-u_1^{(j+1)}\right]+k_2\left[u_1^{(j)}-u_2^{(j)}\right]=0, \tag{1a}$$

$$m_2\frac{d^2u_2^{(j)}}{dt^2}+k_2\left[u_2^{(j)}-u_1^{(j)}\right]+k_3\left[u_2^{(j)}-u_3^{(j)}\right]=0, \tag{1b}$$

$$m_3\frac{d^2u_3^{(j)}}{dt^2}+k_3\left[u_3^{(j)}-u_2^{(j)}\right]=0, \tag{1c}$$

where $u_\alpha^{(j)}$ is defined as the displacement of mass "α" (α = 1, 2, or 3) in the jth unit cell of the lattice. Based on the Bloch–Floquet theory,

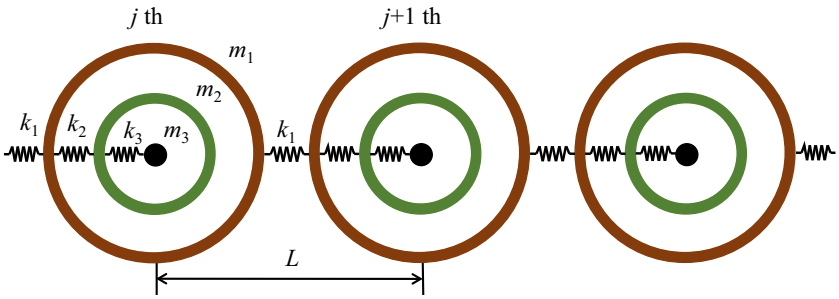

Fig. 1. Non-dissipative mass-in-mass lattice system with two resonators.

the harmonic waveform of the displacement for the $(j+n)$th unit cell is given as

$$u_{\alpha}^{(j+n)} = B_{\alpha} e^{i(qx+nqL-\omega t)}, \tag{2}$$

where B_α is the amplitude of the displacement, q is the wavenumber, and ω is the angular frequency. By substituting Eq. (2) into Eq. (1), wave dispersion relations can be obtained by setting the determinant of the system equal to zero as

$$\begin{vmatrix} -\Omega^2 \frac{\delta_2}{\theta_2} + 2(1-\cos qL) + \delta_2 & -\delta_2 & 0 \\ -\delta_2 & -\Omega^2 \delta_2 + \delta_2 + \delta_3 & -\delta_3 \\ 0 & -\delta_3 & -\Omega^2 \frac{\delta_2 \theta_3}{\theta_2} + \delta_3 \end{vmatrix} = 0, \tag{3}$$

where $\Omega = \omega/\omega_0$ is the non-dimensional frequency with $\omega_0 = \sqrt{k_2/m_2}$. The mass and stiffness ratios are defined as $\theta_2 = m_2/m_1$, $\theta_3 = m_3/m_1$, $\delta_2 = k_2/k_1$ and $\delta_3 = k_3/k_1$.

According to Eq. (3), three branches of the band structure can be obtained, which is shown in Fig. 2(a). In the figure, mass and stiffness ratios, θ_2, θ_3, δ_2 and δ_3 are selected to be 2.0, 8.0, 0.05 and 0.05, respectively. For this case, ω_0 is assumed to be $\sqrt{0.025k_1/m_1}$, and unchanged in following analyses of this paper. Two bandgaps can be observed (shaded area in the figure) in the low-frequency ranges of $\omega = 0.34\omega_0 \sim 0.89\omega_0$ and $\omega = 1.46\omega_0 \sim 1.86\omega_0$, where waves cannot propagate through the lattice system. As also observed from the figure, a passband exists between these two bandgaps, in which no wave attenuation can be found.

If we consider this multi-resonator lattice system to be represented by a monatomic lattice system with single masses, m_{eff}, connected by spring elements with coefficient k_1, the dispersion equation of this homogeneous lattice system should satisfy the dispersion relations given in Eq. (3). Thus, m_{eff} is readily obtained as

$$m_{eff} = \frac{2k_1(1-\cos qL)}{\omega^2}. \tag{4}$$

The dimensionless effective mass m_{eff}/m_1 in function of frequency is plotted in Fig. 2(b) for the same material constants used in Fig. 2(a). By comparing Fig. 2(b) with Fig. 2(a), it can be found that frequency regimes of the two bandgaps can almost be interpreted and predicted by the frequency regimes of the negative effective mass density, which implied that the wave energy must be transferred and stored into negative motions of the inner masses instead of propagating along the lattice system and as a consequence the negative mechanical motions (inertia forces) block or reflect the incoming wave.

In order to reveal the mechanical transfer mechanism of inner masses, the dimensionless displacement amplitudes of inner masses, m_2 and m_3, are calculated from the eigenvectors of Eq. (3) and shown in Fig. 2(c) and (d), respectively, where material constants are left unchanged as those used in Fig. 2(a) and (b). It is interesting to note that both u_2 and u_3 are in phase with u_1 at

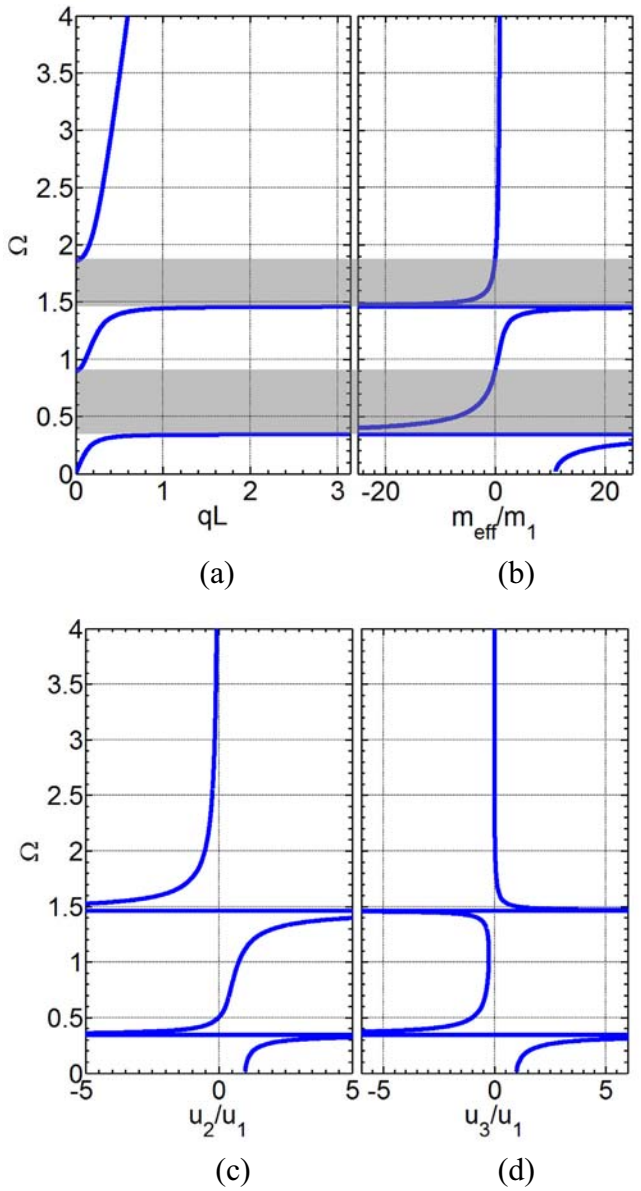

Fig. 2. (a) Band structure of a non-dissipative lattice system with two resonators; (b) effective mass of a non-dissipative lattice system with two resonators; (c) dimensionless wave displacement amplitude of m_2 in a non-dissipative lattice system with two resonators; (d) dimensionless wave displacement amplitude of m_3 in a non-dissipative lattice system with two resonators.

frequencies lower than the first resonant frequency. However, when the frequency increases and occupies the region between the first and the second resonant frequencies, u_2 is initially out of

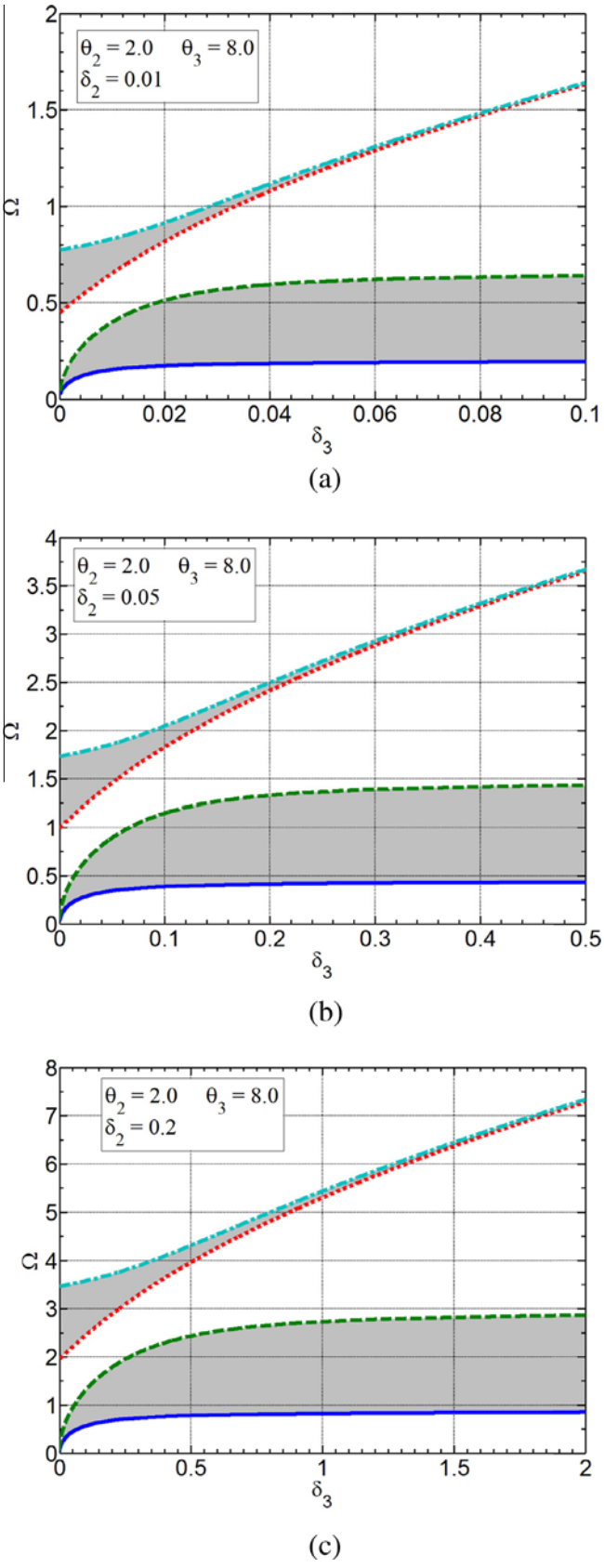

Fig. 3. Bandgap variations of a non-dissipative two resonator lattice system with different stiffness ratios ($\theta_2 = 2.0$, $\theta_3 = 8.0$): (a) $\delta_2 = 0.01$; (b) $\delta_2 = 0.05$; (c) $\delta_2 = 0.2$.

phase with u_1 and then gradually becomes in phase with u_1, while u_3 is always out of phase with u_1. Therefore, by comparing Fig. 2(c) and (d) with Fig. 2(a) and (b), it can be concluded that (1) in the first bandgap, m_2 and m_3 work together to block the incoming wave through their out of phase inertial forces; (2) in the second bandgap, u_2 becomes out of phase with u_1 again, and u_3 becomes in phase with u_1, therefore, only m_2 works to suppress the incoming wave through its own out of phase inertia force in the second bandgap region. These findings will be useful for the microstructure design of the metamaterial to achieve multiple bandgaps in the desired frequency regimes.

2.2. Bandgap design of the non-dissipative lattice system

Bandgap edge frequencies of the non-dissipative EMM counterpart are then characterized. Attention is paid to the effects of the microstructure parameters on locations and widths of multiple bandgap frequencies. In the analysis, a weight constraint of the metamaterial is applied by fixing the total weight of the system for practical application.

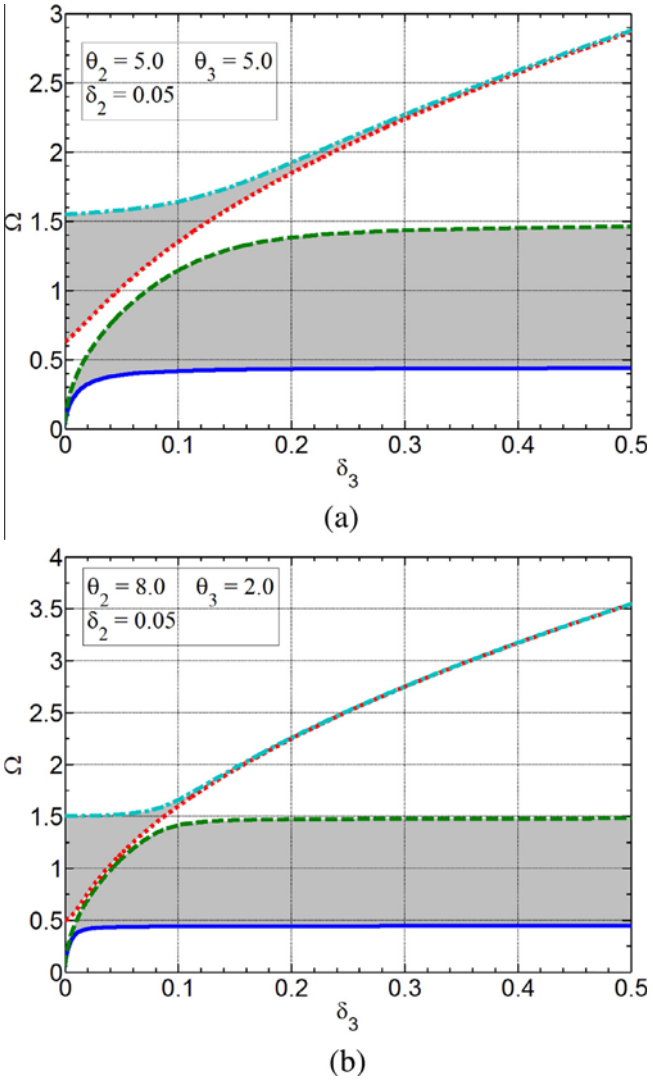

Fig. 4. Bandgap variations of a non-dissipative two resonator lattice system with different mass ratios ($\delta_2 = 0.05$): (a) $\theta_2 = 5.0$, $\theta_3 = 5.0$; (b) $\theta_2 = 8.0$, $\theta_3 = 2.0$.

Fig. 3 shows the variation of bandgap edge frequencies of the non-dissipative system with two resonators with different stiffness ratios. In the figures, the weight constraint is considered by assuming two mass ratios of the inner masses (resonators) as $\theta_2 = 2.0$ and $\theta_3 = 8.0$, respectively. Solid and dotted curves represent lower edge frequencies of the first and second bandgaps, respectively, and dashed and dash-dot curves denote upper edge frequencies of the first and second bandgaps, respectively. Shaded areas denote bandgap regions. Effects of both stiffness ratios δ_2 and δ_3 on bandgap edge frequencies are investigated in Fig. 3(a)–(c) by assuming $\delta_2 = 0.01$, 0.05 and 0.2, respectively. In each figure, the variation of the bandgap edge frequencies with the change of the stiffness ratio δ_3 is illustrated. As can be seen in the three figures, when δ_3 is increased, the width of the first bandgap becomes larger, while the width of the second bandgap becomes smaller. As shown in Fig. 3(a)–(c), it is worth noting that the dimensionless locations and widths of the two bandgaps are directly related to the ratio, δ_3/δ_2.

For example, when δ_3 approaches δ_2, the gap of the passband between the first and the second bandgaps becomes the smallest one. Thus, in order to more easily connect or merge these two bandgaps into one large attenuation region through properly selecting damping elements, it is suggested to select the value of δ_3 around the value of δ_2.

The mass ratio effects upon the variation of bandgap edge frequencies of the non-dissipative system is further investigated by fixing $\delta_2 = 0.05$ and selecting $\theta_2 = 5.0$; $\theta_3 = 5.0$ and $\theta_2 = 8.0$; $\theta_3 = 2.0$, as shown in Fig. 4(a) and (b), respectively. By comparing the results in Figs. 3(b) and 4, it can be found that the width of a passband between the first and second bandgaps becomes smaller, as the inner-mass ratio parameter, θ_3/θ_2, is decreased from 4.0 to 0.25, which means that the low inner mass ratio parameter θ_3/θ_2 can be used for the design of the two bandgaps to be close to each other. However, it should be mentioned that the total wave attenuation frequency range by merging the two bandgaps could be smaller with the decrease of the inner mass ratio parameter θ_3/θ_2 as shown in those figures. Therefore, the selection of inner mass ratio parameter, which determines the non-dissipative bandgap patterns, will be primarily important for the design of a dissipative EMM to form a broadband wave mitigation.

3. Dissipative mass-in-mass lattice system with multiple resonators

3.1. Wave dispersion of the dissipative lattice system

As discussed in the non-dissipative system, the wave energy is actually stored only temporarily by the internal masses (resonators) and requires the external forcing agent to absorb it. It was found that tailoring the damping in the microstructural resonator can enhance attenuation and absorption characteristics of the metamaterials with one resonator [20]. In order to merge the multiple bandgaps presented in the previous non-dissipative system and form a complete broadband wave mitigation region, three damping elements are introduced into each unit cell of the 1D dissipative mass-in-mass lattice system and the results are shown in Fig. 5. In the figure, c_1 is denoted as the damping coefficient of the host medium, and c_2 and c_3 represent the damping coefficients of the middle and innermost resonators within each unit cell, respectively. For the dissipative system, equations of motion are written as

$$m_1\frac{d^2u_1^{(j)}}{dt^2} + k_1\left[2u_1^{(j)} - u_1^{(j-1)} - u_1^{(j+1)}\right] + c_1\left[2\frac{du_1^{(j)}}{dt} - \frac{du_1^{(j-1)}}{dt} - \frac{du_1^{(j+1)}}{dt}\right] + k_2\left[u_1^{(j)} - u_2^{(j)}\right] + c_2\left[\frac{du_1^{(j)}}{dt} - \frac{du_2^{(j)}}{dt}\right] = 0, \tag{5a}$$

$$m_2\frac{d^2u_2^{(j)}}{dt^2} + k_2\left[u_2^{(j)} - u_1^{(j)}\right] + c_2\left[\frac{du_2^{(j)}}{dt} - \frac{du_1^{(j)}}{dt}\right] + k_3\left[u_2^{(j)} - u_3^{(j)}\right] + c_3\left[\frac{du_2^{(j)}}{dt} - \frac{du_3^{(j)}}{dt}\right] = 0, \tag{5b}$$

$$m_3\frac{d^2u_3^{(j)}}{dt^2} + k_3\left[u_3^{(j)} - u_2^{(j)}\right] + c_3\left[\frac{du_3^{(j)}}{dt} - \frac{du_2^{(j)}}{dt}\right] = 0. \tag{5c}$$

By substituting Eq. (2) into Eq. (5) as we did for the non-dissipative lattice system, wave dispersion relations of the dissipative lattice system can be obtained as

$$\begin{vmatrix} A_{11} & A_{12} & A_{13} \\ A_{21} & A_{22} & A_{23} \\ A_{31} & A_{32} & A_{33} \end{vmatrix} = 0, \tag{6}$$

in which

$$A_{11} = -\Omega^2\frac{\delta_2}{\theta_2} + 2(1-\cos qL)\left(1 + i\Omega\tau_1\sqrt{\frac{\delta_2}{\theta_2}}\right) + \delta_2(1 + i\Omega\tau_2), \tag{7a}$$

$$A_{12} = A_{21} = -\delta_2(1 + i\Omega\tau_2), \tag{7b}$$

$$A_{13} = A_{31} = 0, \tag{7c}$$

$$A_{22} = -\Omega^2\delta_2 + \delta_2(1 + i\Omega\tau_2) + \delta_3 + i\Omega\tau_3\sqrt{\frac{\delta_2\delta_3\theta_3}{\theta_2}}, \tag{7d}$$

$$A_{23} = A_{32} = -\delta_3 - i\Omega\tau_3\sqrt{\frac{\delta_2\delta_3\theta_3}{\theta_2}}, \tag{7e}$$

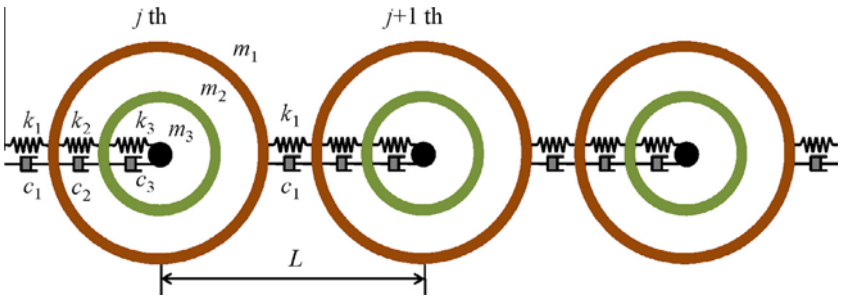

Fig. 5. Dissipative mass-in-mass lattice system with two resonators.

$$A_{33} = -\Omega^2 \frac{\delta_2\theta_3}{\theta_2} + \delta_3 + i\Omega\tau_3\sqrt{\frac{\delta_2\delta_3\theta_3}{\theta_2}}, \tag{7f}$$

and the dimensionless damping coefficient is defined as $\tau_i = c_i \Big/ \sqrt{k_i m_i}$.

According to Eq. (6), the dimensionless wavenumber, qL, will be complex when given a real frequency, ω, and when damping effects appear in the lattice system. As a result, the wave will be attenuated spatially during propagation in the dissipative EMM. The dimensionless wavenumber can then be described by $qL = \alpha + i\beta$, where α and β represent the propagation and attenuation/dissipation portions of the wave, respectively. For the current dissipative system, the wave attenuation and dissipation behavior will be insured by the coupling of local resonant motions and the inner damping. Specifically, the imaginary part of the wavenumber of the system, termed as "attenuation factor", will be studied to evaluate the magnitude of the attenuation/dissipation performance with the change of the damping values of the system.

Fig. 6 shows the imaginary part of the wavenumber of the dissipative mass-in-mass lattice system with different inner damping coefficients. Effects of the background material damping coefficient τ_1 are outside the scope of this study, and thus is assumed to be zero. In the figure, the stiffness ratios are assumed to be $\delta_3 = \delta_2 = 0.05$, mass ratios are $\theta_2 = 2.0$ and $\theta_3 = 8.0$. As illustrated in Fig. 6(a), for the case of $\tau_2 = 0.01$ and variation of τ_3, two clear wave attenuation regions can be observed (solid curve) at two bandgap frequencies, where the effective masses are negative as shown in Fig. 2(b) when the innermost damping coefficient is a small value ($\tau_3 = 0.01$). When τ_3 is increased to 0.2 (dashed curve), it is interesting to find that the imaginary part of the wavenumber is dramatically increased for the original passband frequencies between the two bandgaps and a broad frequency region with reasonable wave attenuation is formed by merging the two bandgap frequencies. A broad wave attenuation frequency range can be still observed when τ_3 is increased further to 1.0 (dotted curve). However, the magnitude of β at the second bandgap frequencies is significantly decreased, and thus a narrower wave attenuation bandwidth is expected compared with the case for $\tau_3 = 0.2$. Fig. 6(b) shows the variation of the imaginary part of the wavenumber with the change of τ_3 for the case of $\tau_2 = 0.1$. Similar wave attenuation phenomena can also be observed and wave attenuation ability is enhanced mostly for the wave frequencies higher than the second bandgap with the increase of the damping coefficient τ_2. Therefore, the innermost damper with optimal damping coefficient τ_3 is a key factor and should be carefully selected to achieve low-frequency wave attenuation. Fig. 6(c) shows the variation of the imaginary part of the wavenumber with the change of τ_3 for the case of $\tau_2 = 1.0$. It is found that the imaginary part of the wavenumber is actually decreased for the wave frequencies below the second bandgap compared with the cases of small values of τ_2, which further validate that the high damping coefficient τ_2 is not desirable for the low-frequency attenuation. For this case, only wave components higher than the second bandgap frequency can be efficiently attenuated with the increase of the damping coefficient τ_2.

To illustrate the mass ratio's effects, Fig. 7 shows the imaginary part of the wavenumber of the dissipative mass-in-mass lattice system with different inner damping coefficients. In the figure, the mass ratios are selected as $\theta_2 = 8.0$ and $\theta_3 = 2.0$, and the stiffness ratios are the same as those in Fig. 6. As shown in Fig. 7(a), the passband frequency region between the two bandgaps becomes narrower (solid curve) compared with that in Fig. 6(a), when the two inner damping coefficients are small values ($\tau_2 = \tau_3 = 0.01$). For this case, it can be found that a broadband wave attenuation range can be easily formed by increasing the innermost damping coefficient τ_3 to 0.2 and 1.0 (dashed and dotted curves). The absolute value of the imaginary part of the wavenumber at the frequencies between two bandgaps is very uniform and

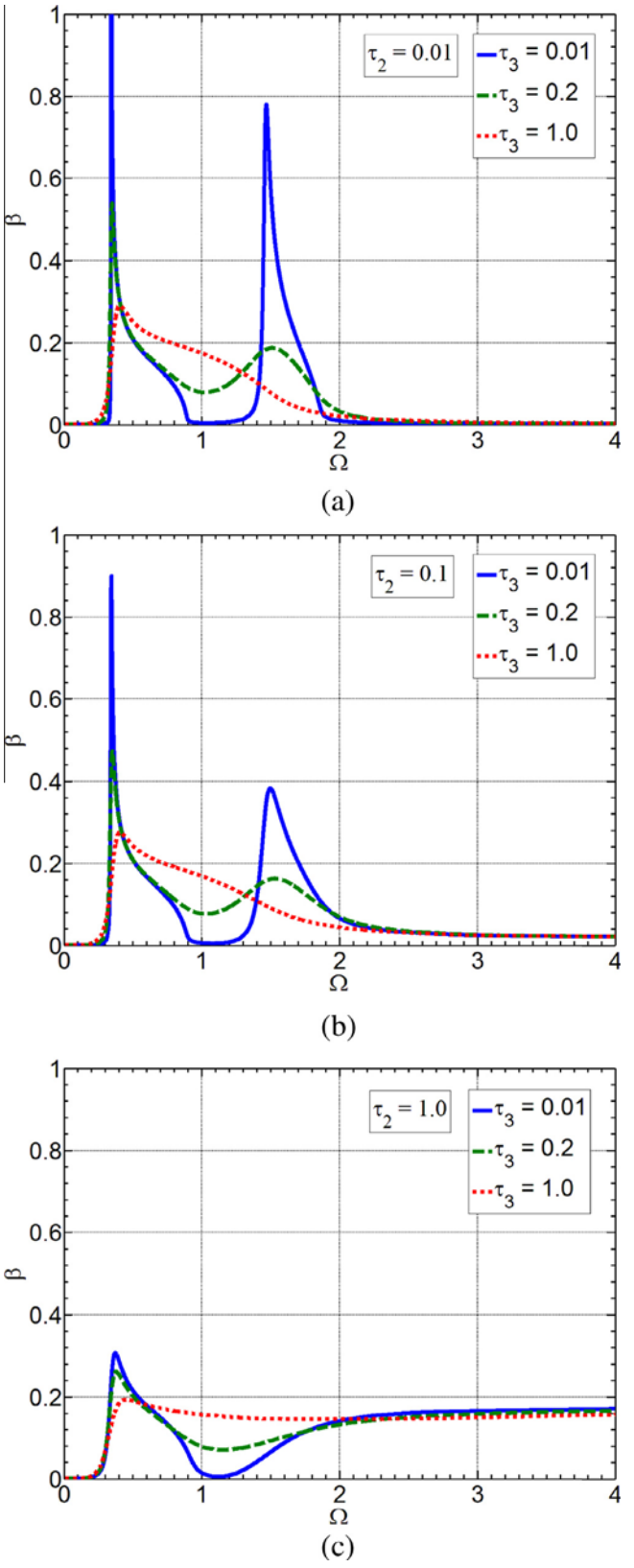

Fig. 6. Imaginary part (attenuation constant) of wavenumber of a dissipative two resonator lattice system with different damping coefficients ($\theta_2 = 2.0$, $\theta_3 = 8.0$, $\delta_2 = \delta_3 = 0.05$): (a) $\tau_2 = 0.01$; (b) $\tau_2 = 0.1$; (c) $\tau_2 = 1.0$.

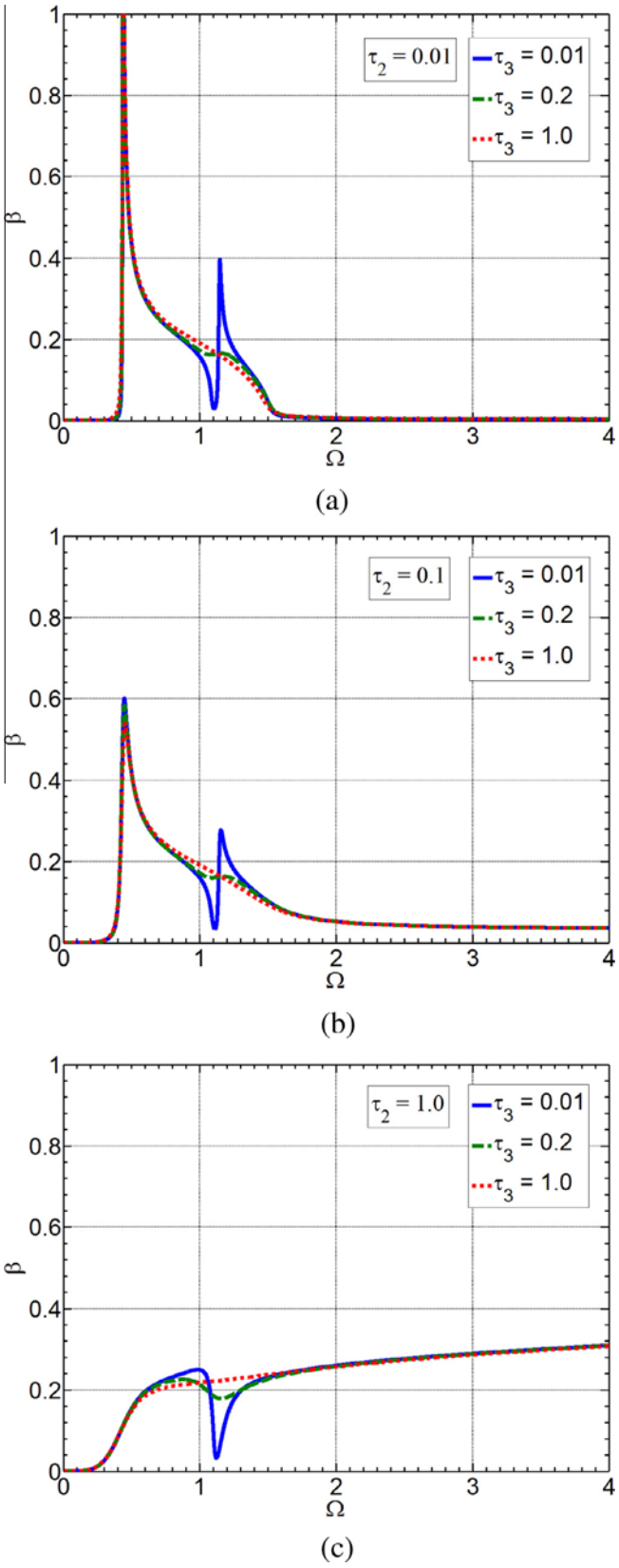

Fig. 7. Imaginary part (attenuation constant) of wavenumber of a dissipative two resonator lattice system with different damping coefficients ($\theta_2 = 8.0$, $\theta_3 = 2.0$, $\delta_2 = \delta_3 = 0.05$): (a) $\tau_2 = 0.01$; (b) $\tau_2 = 0.1$; (c) $\tau_2 = 1.0$.

close to the values within the bandgaps. For the cases of $\tau_3 = 0.2$ and 1.0, wave attenuation behaviors in the combined attenuation bands are almost identical. To compare, Fig. 7(b) and (c) shows variations of the imaginary part of the wavenumber of the dissipative mass-in-mass lattice system with the change of the damping coefficient τ_2. It is found that when τ_2 is increased, wave attenuation at frequencies higher than the second bandgap can be significantly improved, which is reflected by the fact of higher values of the imaginary part of the wavenumber. To understand the unique wave attenuation behaviors induced by τ_2 and τ_3, the mechanical motions of the two resonators, as shown in Fig. 2(c) and (d), are revisited. From the two figures, it can be noted that m_2 and m_3, which are connected by the innermost dashpot with the damping coefficient τ_3, move out of phase at frequencies between two bandgaps. It is believed that the energy absorption due to damping effects can be significant improved by the out of phase motions at two ends of the dashpot, therefore, the damping coefficient τ_3 can effectively cause the wave attenuation behaviors in this passband region. Similarly, m_2 moves out of phase with m_1 in the frequency region higher than the second bandgap, thus, the damping coefficient τ_2 will be more efficient to tailor the wave attenuation behaviors at higher frequencies.

3.2. Effective modeling of the dissipative lattice system

To quantitatively reveal and identify the actual working mechanisms of the coupling effects from the mechanical motion and damping in the dissipative system, an effective monatomic lattice model is developed, which shown in Fig. 8. Due to the inner damping effects, the effective monatomic lattice for the dissipative lattice system contains not only a single effective mass m_{eff} to represent wave energy transferred or temporally stored but also an effective metadamping c_{eff} to represent wave energy absorption.

The equation of motion of the single mass in the dissipative monatomic lattice system at the jth unit cell is

$$m_{eff}\frac{d^2u_1^{(j)}}{dt^2} + k_1\left[2u_1^{(j)} - u_1^{(j-1)} - u_1^{(j+1)}\right] + c_1\left[2\frac{du_1^{(j)}}{dt} - \frac{du_1^{(j-1)}}{dt} - \frac{du_1^{(j+1)}}{dt}\right] + c_{eff}\frac{du_1^{(j)}}{dt} = 0. \tag{8}$$

The dispersion equation for harmonic waves can be readily obtained as

$$\omega^2 m_{eff} = 2(k_1 + i\omega c_1)(1 - \cos qL) + i\omega c_{eff}. \tag{9}$$

Physically, both the effective mass m_{eff} and the effective metadamping coefficient c_{eff} are real numbers in nature. According to Eq. (9), wave attenuation caused by the negative mass and the damping absorption can be fully decoupled and quantitatively identified as

$$m_{eff} = \frac{\mathrm{Re}[2(k_1 + i\omega c_1)(1 - \cos qL)]}{\omega^2}, \tag{10a}$$

$$c_{eff} = \frac{\mathrm{Im}[-2(k_1 + i\omega c_1)(1 - \cos qL)]}{\omega}. \tag{10b}$$

To clearly demonstrate the two wave attenuation mechanisms, the variation of the dimensionless effective mass and metadamping coefficient with the change of the innermost damping coefficient is presented in Fig. 9. In the figure, the optimal microstructure parameters of the dissipative lattice system, obtained in the previous section, are selected as the mass ratios being $\theta_2 = 2.0$ and $\theta_3 = 8.0$, the stiffness ratios being $\delta_3 = \delta_2 = 0.05$ and the inner damping coefficient being $\tau_2 = 0.01$. As shown in Fig. 9(a), the effective mass becomes negative in the two bandgap frequency regions (solid curves) with a small damping coefficient ($\tau_3 = 0.01$), which means that the out of phase mechanical resonant motions are responsible for the wave attenuation in those frequency regimes. However, the effective metadamping coefficient

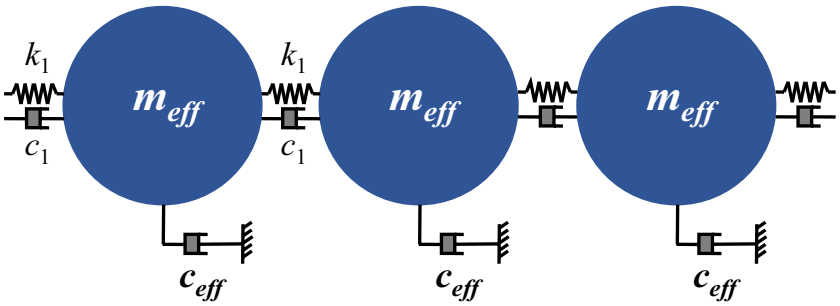

Fig. 8. Dissipative lattice system with two resonators represented by an infinite effective lattice model.

becomes extremely high near the two resonant frequencies, and almost zero at other frequencies. This global metadamping phenomenon in the dissipative metamaterial can be interpreted as the most kinematic energy is stored in the resonators around resonant frequencies and is then efficiently absorbed by using the constitutive medium with very small damping coefficient. However, when the frequency is away from the resonant frequencies, the effective metadamping coefficient of the dissipative metamaterial becomes very small and therefore most of wave energy is attenuated by the locally resonant motions of the inner masses. When τ_3 is increased to 0.2, the effective mass in the first bandgap frequency range is still large negative values, however, the effective mass in the second bandgap frequency range becomes very small negative values and remains positive between the two bandgap frequencies (dashed curves). This means that the wave attenuation ability due to the resonant motions is reduced with the increase of the damping coefficient τ_3, as we expected. However, the metadamping phenomenon could still be observed around the two bandgap frequency ranges and much broader. For the passband frequency range between the two bandgaps especially, the effective metadamping coefficient increases significantly from zero to around 0.25. Therefore, the wave attenuation or absorption mechanism in this passband and the second stopband frequency ranges is essentially due to the damping absorption within the innermost resonator, and the wave attenuation or absorption mechanism in the first bandgap is caused by the coupling mechanism between the mechanical resonant motions and metadamping effects. As a consequence, broadband wave attenuation and absorption can be accomplished by properly selecting the damping coefficient and microstructure parameters of the dissipative metamaterial. As also shown in Fig. 9, when τ_3 is increased to 1.0 (dotted curve), the effective mass in the first bandgap and the proceeding passband frequency ranges becomes negative values, however, the effective mass in the second bandgap frequency range becomes positive values. On the other hand, the effective metadamping coefficient increases significantly in the low-frequency range compared with the cases with small τ_3, and decreases dramatically in the high-frequency range, such as the frequency range of the second bandgap. For this case, a complete wave attenuation and absorption frequency range can still be achieved but in a relative narrow band because the second stopband becomes a passband with a small attenuation factor.

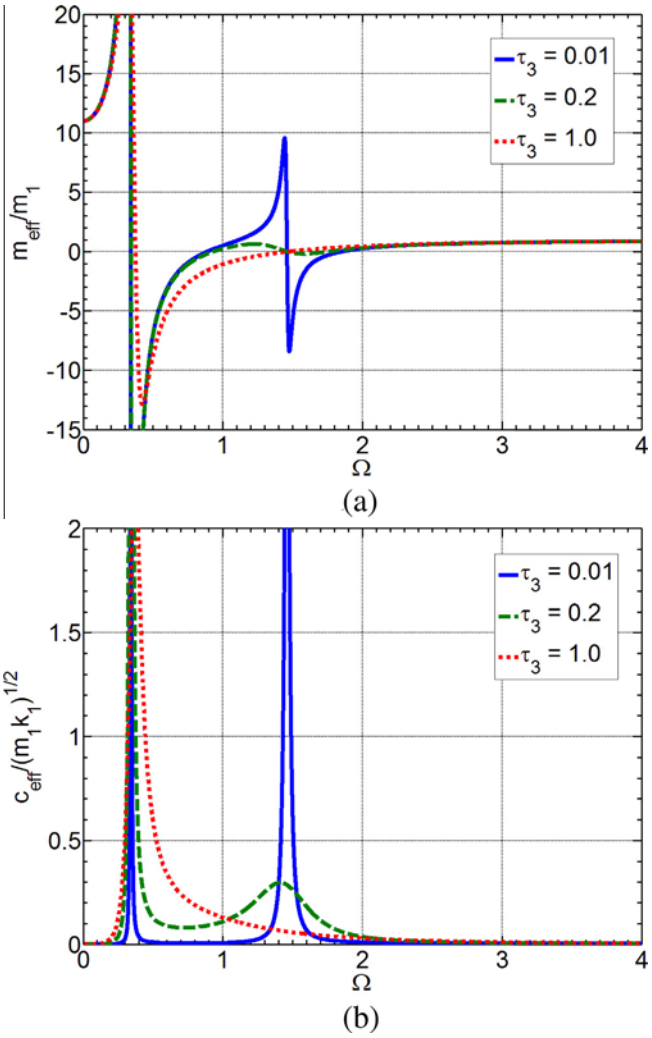

Fig. 9. Effective material parameters of a two resonator dissipative lattice system ($\theta_2 = 2.0$, $\theta_3 = 8.0$, $\delta_2 = \delta_3 = 0.05$, $\tau_2 = 0.01$): (a) effective mass; (b) effective metadamping coefficient.

As a comparison, Fig. 10 shows the variation of the dimensionless effective mass and metadamping coefficient with the change of the innermost damping coefficient for the mass ratios being $\theta_2 = 8.0$ and $\theta_3 = 2.0$ and other material properties left the same. As shown in Fig. 10, when τ_3 is increased to 0.2, it is interesting to find that the effective mass becomes negative between the two bandgap frequencies (dashed curves) and still remains the negative value at second bandgap frequency range although the absolute value is much smaller. However, the metadamping phenomenon can only be observed around the first resonate frequency and the effective metadamping coefficient is very small at other frequencies. Therefore, the wave absorption working mechanism can only be found for the frequencies around the first resonant frequency, and the mechanical resonant motions will play a dominant role for the wave attenuation or blocking at other frequencies, which is not desirable for the design of the dissipative metamaterial. The similar wave attenuation mechanism can also be observed when τ_3 is increased to 1.0.

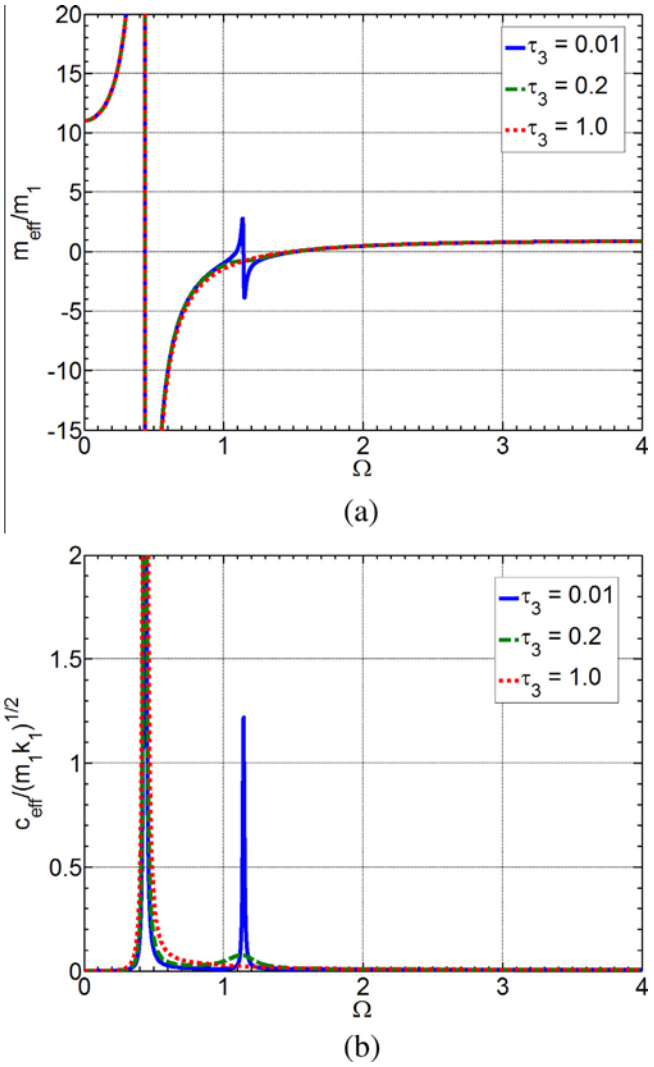

Fig. 10. Effective material parameters of a two resonator dissipative lattice system ($\theta_2 = 8.0$, $\theta_3 = 2.0$, $\delta_2 = \delta_3 = 0.05$, $\tau_2 = 0.01$): (a) effective mass; (b) effective metadamping coefficient.

3.3. Transient analysis under blast loadings

Now we move on to analysis for potential applications of the dissipative EMM for blast wave attenuation by realizing the combination of two bandgaps into a large wave attenuation band by implementing a proper value of the innermost damping coefficient. The ratio θ_3/θ_2 will be selected as a relatively large value to ensure a broadband absorption for blast wave applications. Fig. 11 shows a 1D lattice system for a time domain blast wave transmission test, where the proposed dissipative mass-in-mass lattice system with 15 unit cells is sandwiched between two background materials. The first 400 unit cells contain masses, m_1, and springs, k_1, which are considered incident background material in the left side of the dissipative mass-in-mass lattice system, and the last 385 identical unit cells are denoted as transmitted background material in the right side of the dissipative mass-in-mass lattice system. An incident blast wave is applied as a force signal to the first unit cell of the lattice system using the following equation:

$$F = F_{\max} e^{-\frac{t-t_0}{t_d}}, \tag{11}$$

where $F_{\max} = 1000$ N, $t_0 = 0.5$ ms, and $t_d = 0.1$ ms in order to realistically represent a typical air blast [17]. The frequency domain of the incident signal is calculated in Fig. 12 (solid curve) using the Fast Fourier Transform (FFT) for understanding blast wave properties. It is apparent that the blast wave is broadband with frequencies from 0 to ~10 kHz with large amplitudes in the low-frequency region and weak amplitudes in the higher frequency ranges. To efficiently mitigate such a blast wave, material parameters of the dissipative lattice system are designed and selected as $m_1 = 0.002$ kg, $m_2 = 0.01$ kg, $m_3 = 0.04$ kg, $k_1 = 7.90 \times 10^6$ N/m, $k_2 = 1.58 \times 10^6$ N/m, $k_3 = 7.90 \times 10^5$ N/m, $c_1 = 1.26$ Ns/m, $c_2 = 1.26$ Ns/m and $c_3 = 125.66$ Ns/m.

The frequency domain of the transmitted signal in the proposed dissipative lattice system subjected to a blast pulse is then calculated in Fig. 12 (dotted curve). For comparison, the transmitted signal in the proposed lattice system without damping elements is also plotted in Fig. 12 (dashed curve). For the non-dissipative lattice system (dashed curve), we can see two frequency amplitude dips present at approximately 600–1200 Hz and 2400–4600 Hz. Waves with frequency components within these two regions will be blocked by the non-dissipative mass-in-mass lattice system through mechanical resonant motions and cannot propagate through. However, a large portion of the wave energy can still transmitted through the lattice system, when the frequency component falls between these two dips (i.e. 1200–2400 Hz). As shown in the figure, the dissipative mass-in-mass lattice system can merge the two transmission dips and a broadband wave

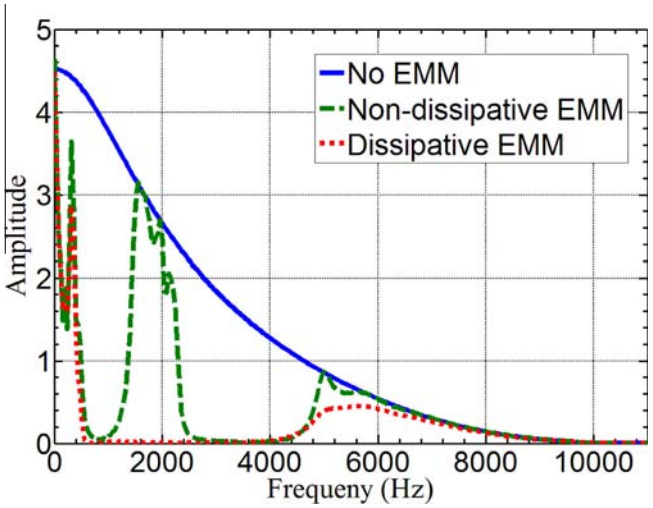

Fig. 12. Frequency domain of blast simulations calculated by Fast Fourier Transform.

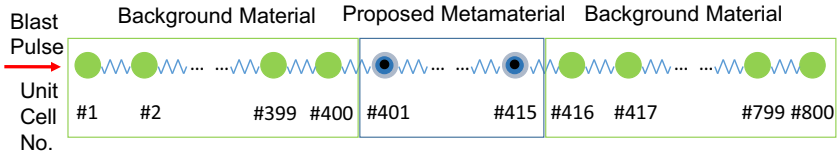

Fig. 11. Schematic design of time domain transmission analysis of a 1-D dissipative mass-in-mass lattice system under a blast incidence.

absorption from 600 Hz to 4600 Hz is clearly observed. As discussed in Section 3.2, for this case, the metadamping plays a dominant role for the wave absorption at frequencies between the two transmission dips. It can be concluded that the proposed dissipative mass-in-mass lattice system is an efficient candidate material for blast wave mitigation.

4. Microstructural design of dissipative EMMs for blast wave mitigation

Recently, research on blast induced shockwaves behavior in various homo and heterogeneous materials has been conducted with the goal of developing practical mechanisms for blast/shockwave mitigation. The topical interest has been brought about due to an array of integrative applications including civilian and military utilizations, both focused on efficient blast/shockwave attenuation. The previous mitigation mechanisms are either based on the deformation of materials to absorb energy [22] or utilizing the anti-momentum principle to oppose or redirect the incoming blast wave [23–25], which results in extensive material damage or complex structures. Furthermore, based on these concepts, wave attenuation cannot be tailored in specific low-frequency regions, and cover the full frequency range of the blast wave.

In this section we propose a microstructure design of the dissipative EMM made of continuum media and its application for blast wave mitigation. We consider a plane strain problem with a unit cell shown in Fig. 13, where material 1 represents the background material that allows for wave propagation. While material 1 represents the outside rigid mass, m_1, and the spring, k_1, the inner two rigid masses are represented by materials 3 and 5 and act as the resonators. Material 2 and 4 represent two kinds of softer materials with damping properties, and are used as coatings to separate the rigid masses acting as springs and dashpots. Each material's thickness is denoted with a radial value from the center of the coatings, R_n, where n denotes the particular layer of material (n = 1, 2, 3, or 4 from outside to inside). The overall length of the unit cell is denoted as L_1, which represents the dimension of the material 1 in which the resonating and dissipative materials are embedded.

4.1. Dispersion calculation by Finite Element Method (FEM)

To determine wave dispersion properties of a periodic structure with FEM, the eigenfrequencies are usually calculated based on the wavenumbers given in Bloch periodic boundary conditions.

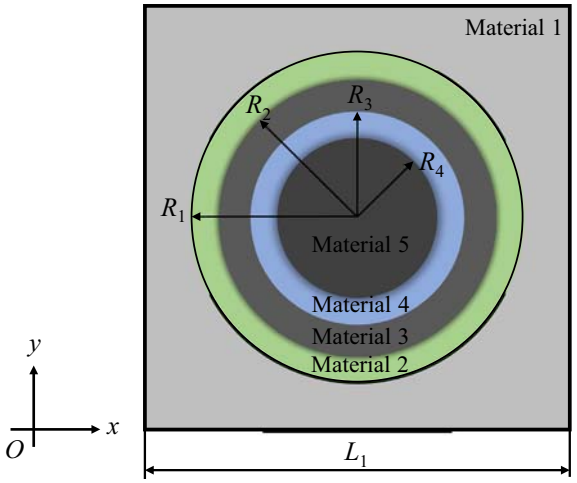

Fig. 13. Microstructure design of a dissipative EMM embedded with two resonators.

However, if the material damping is present, the eigenfrequencies obtained will become complex due to the usage of complex material parameters. These complex eigenfrequencies do not have a clear physical meaning because they are real numbers in nature and cannot represent the overall wave attenuation in space. Additionally, when the damping coefficient is dependent on the frequency, procedures with conventional dispersion analysis will be extremely complicated and special iterative methods need to be developed. Therefore it is an objective to propose a wavenumber calculation method based on given frequencies for periodic structures with damped and/or frequency dependent material properties. Once the complex wavenumber is calculated, wave propagation and attenuation properties can then be easily characterized.

For the plane strain problem, the governing equation (Navier's equation) of motion expressed with displacements is

$$(\lambda+\mu)\nabla\nabla\cdot\mathbf{u}+\mu\nabla^2\mathbf{u}=\rho\ddot{\mathbf{u}}, \tag{12}$$

where $\mathbf{u}=[u_1,u_2]^{\mathrm{T}}$, with u_1 and u_2 being the displacements in the x and y directions, ρ, λ and μ are material mass density, Lamé's first and second constants, respectively, and $\nabla^2=\frac{\partial^2}{\partial x^2}+\frac{\partial^2}{\partial y^2}$.

By considering a primitive cell of the periodic problem and by using the Bloch theorem, the displacement can be assumed as [26]

$$\mathbf{u}=\tilde{\mathbf{u}}e^{i(\mathbf{kx}+\omega t)}, \tag{13}$$

where $\tilde{\mathbf{u}}=[\tilde{u}_1,\tilde{u}_2]^{\mathrm{T}}$ is a periodic function with periodicity being L_1, and $\mathbf{k}=[k_x,k_y]$ with k_x and k_y denoting the wavenumbers in x and y directions. By inserting Eq. (13) into Eq. (12) and letting $\mathbf{k}=[k\cos(\theta),k\sin(\theta)]$ with k and θ being total wavenumber and propagation direction, one can obtain

$$\mathbf{A_2}\tilde{\mathbf{u}}k^2+i\mathbf{A_1}\nabla\tilde{\mathbf{u}}k+(\lambda+\mu)\nabla\nabla\cdot\tilde{\mathbf{u}}+\mu\nabla^2\tilde{\mathbf{u}}+\rho\omega^2\tilde{\mathbf{u}}=0, \tag{14}$$

where

$$\mathbf{A_2}=\begin{bmatrix}-\left[(\lambda+2\mu)\cos^2(\theta)+\mu\sin^2(\theta)\right] & -(\lambda+\mu)\cos(\theta)\sin(\theta)\\ -(\lambda+\mu)\cos(\theta)\sin(\theta) & -\left[(\lambda+2\mu)\sin^2(\theta)+\mu\cos^2(\theta)\right]\end{bmatrix},$$

$$\mathbf{A_1}=\begin{bmatrix}2(\lambda+2\mu)\cos(\theta) & 2\mu\sin(\theta) & (\lambda+\mu)\sin(\theta) & (\lambda+\mu)\cos(\theta)\\ (\lambda+\mu)\sin(\theta) & (\lambda+\mu)\cos(\theta) & 2\mu\cos(\theta) & 2(\lambda+2\mu)\sin(\theta)\end{bmatrix}.$$

For the finite element formulation of Eq. (14), COMSOL Multiphysics is adopted where the periodic boundary condition is applied on the outer boundaries of the unit cell. In order to obtain the dispersion relations of the proposed dissipative EMM, a quadratic eigenvalue problem for k is finally formulated and solved numerically.

The dispersion relations of the longitudinal wave propagated through the proposed dissipative EMM will be numerically determined with $\theta=0$ and the geometric and material properties are listed in Table 1. According to the discussions in Section 3.1, two bandgaps can be combined into one large attenuation band through properly selecting the damping coefficient of the innermost damping coefficient τ_3. This constructive behavior will be continually applied to the dissipative EMM design in this section. For the computational convenience of the application in the time domain analysis, Rayleigh damping coefficient, β_d, is adopted and applied to material 4. The relation between the loss factor and the Rayleigh damping is given as

$$\gamma_d=\omega\beta_d. \tag{15}$$

Fig. 14(a) shows the real portion of the wavenumber of the proposed EMM with the change of the damping coefficient of material 4, which denotes the propagation factor of the longitudinal wave through the EMM. As shown in the figure, two perfect bandgaps

Table 1
Material and geometric parameters of the proposed EMM.

	Material 1	Material 2	Material 3	Material 4	Material 5
Material properties					
Lamé's first constant (Pa)	2.0×10^9	5.0×10^5	2.0×10^{12}	2.0×10^5	2.0×10^{12}
Lamé's second constant (Pa)	1.0×10^9	2.5×10^5	1.0×10^{12}	1.0×10^5	1.0×10^{12}
Density (kg/m^3)	1000.0	1000.0	20000.0	1000.0	20000.0
Geometrical parameters					
L_1 (mm)	R_1 (mm)	R_2 (mm)	R_3 (mm)	R_4 (mm)	
20.0	9.0	8.5	8.0	7.5	

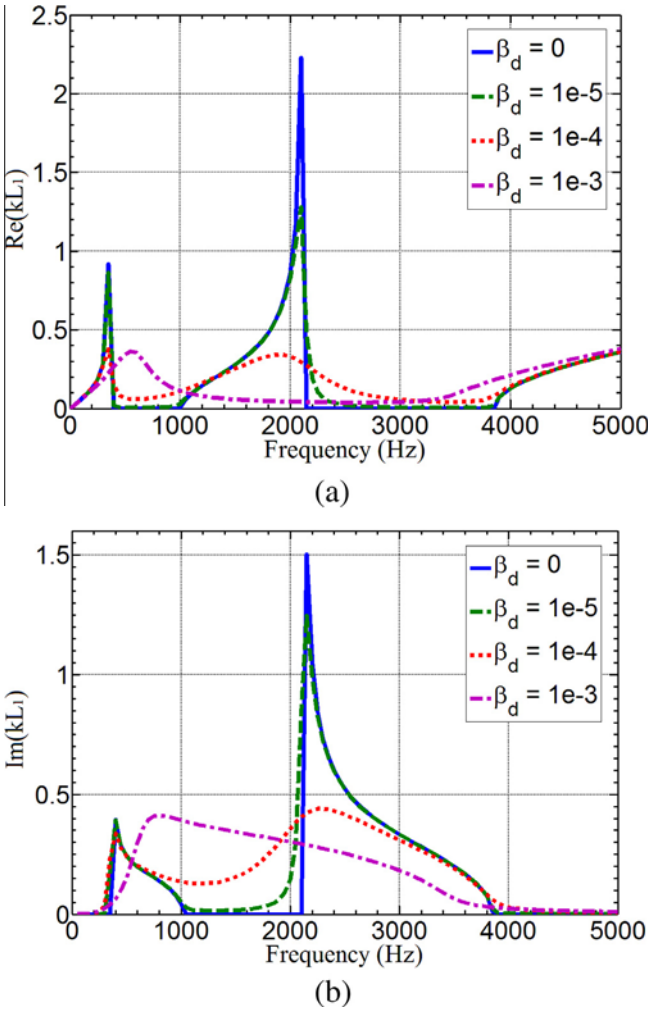

Fig. 14. Dispersion relations of the dissipative EMM embedded with two resonators: (a) real portion of the wavenumber; (b) imaginary portion of the wavenumber.

are present for the frequency ranges of approximately 400–1000 Hz and 2200–3800 Hz for the EMM with zero Rayleigh damping. As the damping magnitude is increased, the bandgaps are removed and the previously evanescent wave ($\mathrm{Re}(kL_1) = 0$) becomes a propagating wave ($\mathrm{Re}(kL_1) \neq 0$) because of the appearance of the damping element. The propagation factor $\mathrm{Re}(kL_1)$ increases with the increase of the damping coefficients. The imaginary portion of the wavenumber is shown in Fig. 14(b). In the figure, we see the two separate wave attenuation regions present for little or no damping cases ($\beta_d = 0$ and 1×10^{-5}). As the Rayleigh damping is increased to 1×10^{-4} and 1×10^{-3}, the attenuation region becomes broad, occupying a frequency range of approximately 400–3800 Hz, which implies that the broadband wave attenuation/dissipation due to the metadamping presented in Section 3 has been realized through a simple embedded EMM design. It should be mentioned that the broadband wave attenuation/dissipation behavior is the consequence of the coupling of the metadamping and local resonant motion of the designed EMM.

4.2. Blast wave mitigation of the proposed dissipative EMM

For practical applications, we also conduct transient analysis of N number of unit cells sandwiched between incident and transmission bars to examine blast wave mitigation of the proposed dissipative EMM, as shown in Fig. 15. The finite element based time domain analysis will be performed, where plane strain assumptions still hold. Material and geometrical parameters for the dissipative EMM have been left unchanged from those used in Fig. 14. The material used in incident and transmission bars is the background material 1 in the dissipative EMM. The length of the two bars is 8 m. A longitudinal incident force of the form, $F = F_0 e^{-\frac{t-t_0}{t_d}}$, is applied to the left edge of the incident bar to generate a blast wave profile, where $F_0 = 100$ N/m, $t_0 = 0.5$ ms and $t_d = 0.2$ ms. The particle velocity at a point 200 mm from the left edge of the incident bar is measured as an incident blast signal. After the blast wave has traveled through the proposed dissipative EMM, the transmitted signal is then measured at a point 50 mm from the Nth cell. All the other outer edges are set free in the numerical simulations. Attention will be focused on determining the total number of unit cells necessary for efficient mitigation of the incoming blast wave.

Fig. 16(a) shows simulated time domain blast wave signals measured on the incident and transmission bars under transmission tests of the proposed EMM with different Rayleigh damping coefficients for 5 unit cells ($N = 5$). The signal presented in the upper window of Fig. 16(a) illustrates a blast wave generated by an applied force on the left end of the incident bar and then reflected on the interface between the incident bar and the EMM. The other windows in Fig. 16(a) demonstrate transmitted signals

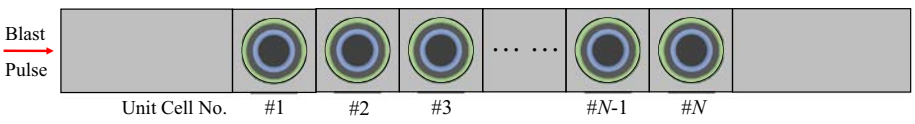

Fig. 15. Schematic design of time domain transmission analysis of the dissipative EMM under a blast incidence.

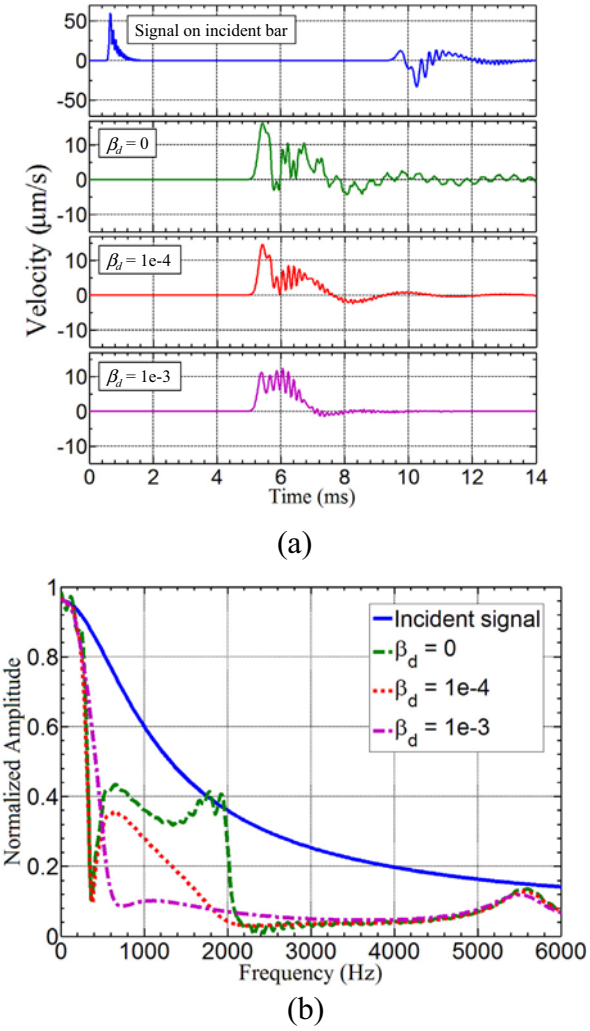

Fig. 16. Signals of blast waves measured on the incident and transmitted bars of the dissipative EMM with 5 unit cells: (a) time domain; (b) frequency domain.

of blast waves traveling through the dissipative EMM with different Rayleigh damping coefficients, β_d = 0, 1e−4 and 1e−3, respectively. It can be found that as the damping coefficient is increased, the peak amplitude of the transmitted signal will be decreased and the transmitted blast wave can be attenuated faster than that with a smaller Rayleigh damping coefficient, β_d. Fig. 16(b) shows the frequency amplitude through FFT of these input and transmitted signals. From Fig. 16(b), we can see that the wave with frequency components within the bandgaps can be successfully mitigated, when the Rayleigh damping is equal to zero, $\beta_d = 0$. Clearly, a passband between the two bandgaps can be also observed. It is worth noting that the frequency range of wave attenuation is slightly higher than the width of the bandgaps that were predicted in Fig. 14. When Rayleigh damping is applied (i.e. $\beta_d = 1 \times 10^{-4}$) to material 4, wave attenuation becomes strong in the lower frequency region. Specifically, waves can be absorbed within the passband frequencies, as predicted in Fig. 14. However, almost no changes are observed for higher frequency values than those that were seen when Rayleigh damping was absent ($\beta_d = 0$). When greater damping is applied (i.e. $\beta_d = 1 \times 10^{-3}$), waves can be adequately mitigated in the frequency range from 600 Hz to 5000 Hz. However, this range is slightly narrower than that in the previous case. In order to further reveal wave behaviors and inner mass motions of the dissipative EMM with 5 unit cells in details, velocity fields of this blast wave at different times (t = 5.12, 5.30, 5.44 and 5.62 ms) are extracted and shown in Fig. 17. In the figure, the Rayleigh damping coefficient, $\beta_d = 1 \times 10^{-4}$, is employed. As shown in Fig. 17, the left side windows represent velocity fields within the whole system, while the right side windows denote velocity fields in the first unit cell. The unit of the color legend is in m/s. It can be observed from Fig. 17(a) that when t = 5.12 ms, the blast wave is approaching the EMM and both the middle and innermost masses are kept motionless. When t = 5.30 ms, as shown in Fig. 17(b), the blast wave has just traveled into the EMM. At this time, the middle mass moves with the background material in the same direction, whereas the innermost mass starts to move but with a much smaller amplitude. It demonstrates that large amounts of the wave energy is starting to flow and be stored in the inner resonators. At the same time, the stored wave energy is also dissipated within the embedded resonators,

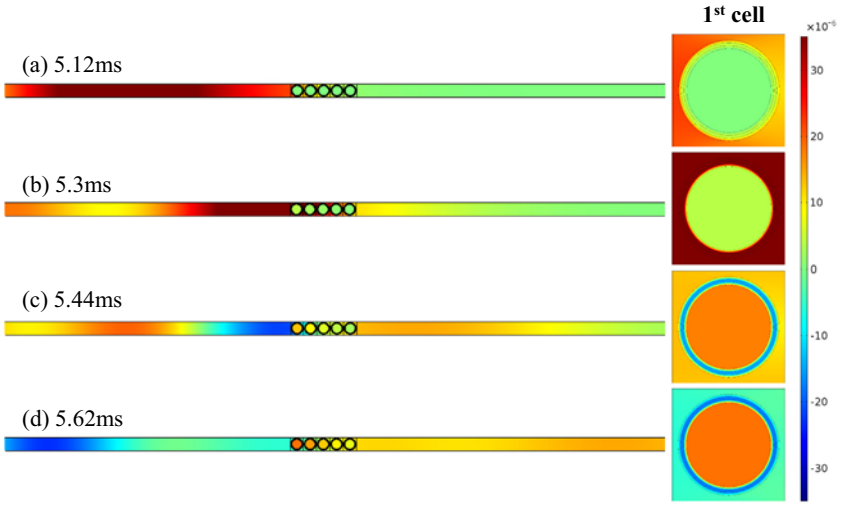

Fig. 17. Velocity fields of the blast wave on the incident and transmitted bars and the dissipative EMM with 5 unit cells at different times: (a) t = 5.12 ms; (b) t = 5.30 ms; (c) t = 5.44 ms; (d) t = 5.62 ms.

due to the damping in material 4. When $t = 5.44$ ms, as shown in Fig. 17(c), the blast wave has just traveled through the EMM. At this time, the middle mass moves in the opposite direction with the innermost mass, which illustrates the stored energy continues to be dissipated within the innermost damping material. When $t = 5.62$ ms, as shown in Fig. 17(d), the blast wave has traveled far from the EMM. At this time, the middle mass still moves in the opposite direction as the innermost mass but with larger amplitudes. As a result, the stored energy in the resonators will be totally absorbed in material 4. Thus, the metadamping behaviors have been clearly illustrated through wave energy transferred and absorbed in time domain.

Effects of the number of unit cells, N, on blast wave mitigation efficiency is examined and illustrated in Figs. 18 and 19. Time domain blast wave signals measured on the incident and transmission bars of the proposed EMM with different Rayleigh damping coefficients are presented in Figs. 18(a) and 19(a), where $N = 10$ and 15, respectively. Comparing Figs. 18(a) and 19(a) with Fig. 16(a), it can be observed that signals on the incident bar with different numbers of unit cells are almost identical. As expected, when the number of unit cells is increased, the peak amplitude of the transmitted signal will decrease, which indicates better attenuation performance with larger number of unit cells. Figs. 18

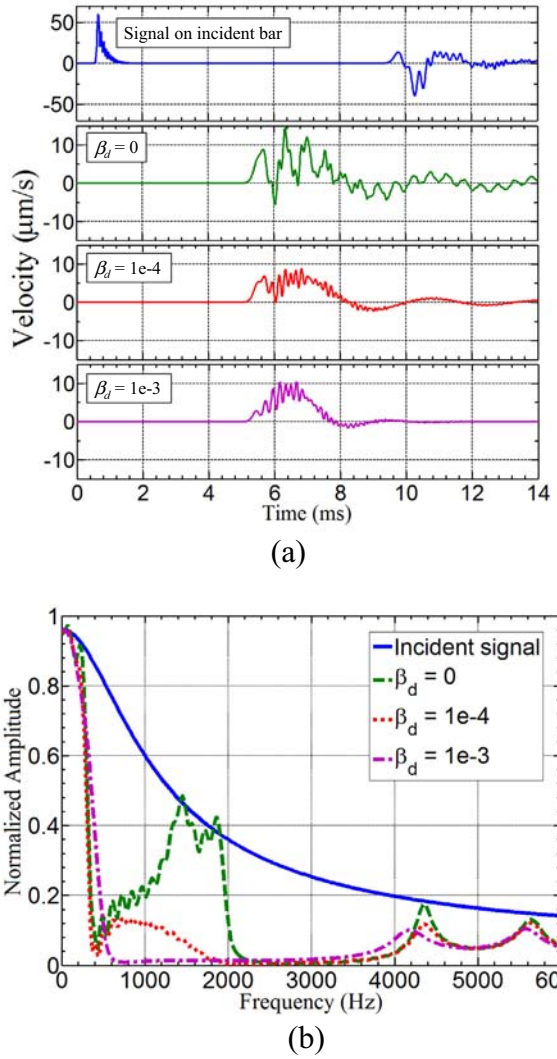

Fig. 18. Signals of blast waves measured on the incident and transmitted bars of the dissipative EMM with 10 unit cells: (a) Time domain; (b) Frequency domain.

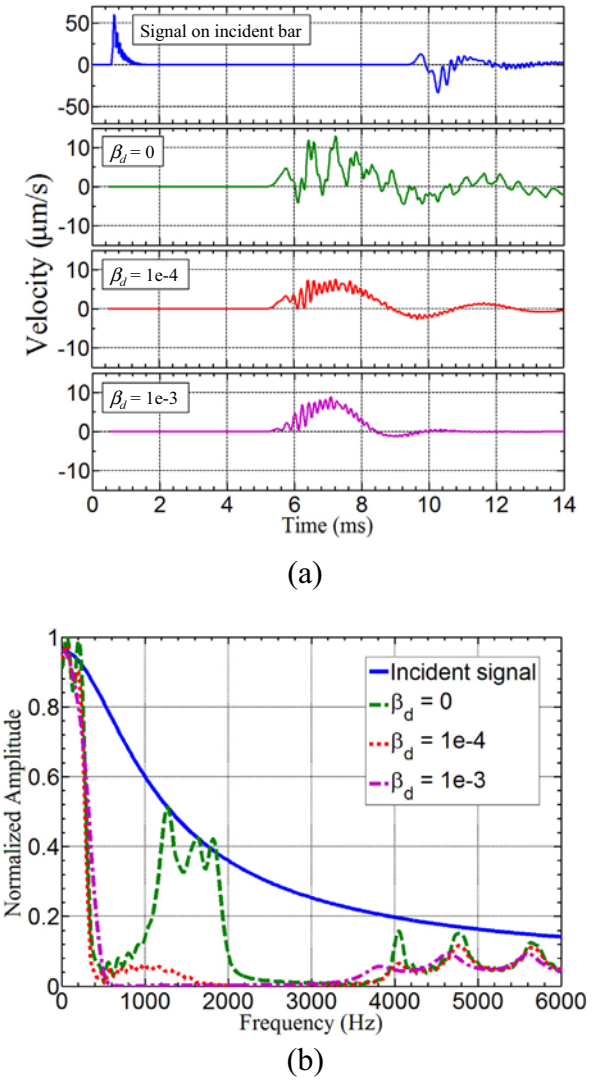

Fig. 19. Signals of blast waves measured on the incident and transmitted bars of the dissipative EMM with 15 unit cells: (a) Time domain; (b) Frequency domain.

(b) and 19(b) show the frequency amplitude through FFT of these input and transmitted signals, when $N = 10$ and 15, respectively. In these two figures, wave attenuation can be significantly improved in a broad frequency region. For example, waves can be almost completely absorbed at frequencies between 400 Hz and 4000 Hz, when $\beta_d = 1 \times 10^{-4}$ and 15 EMM unit cells are employed. The most efficient absorption characteristics usually coincide with large damping parameters, however, the attenuation band will become narrower for $\beta_d = 1 \times 10^{-3}$ compared with those when $\beta_d = 1 \times 10^{-4}$. Optimization of the design is still needed however, as some extremely low-frequency components will remain leaked to the proceeding system.

5. Summary

This paper presents comprehensive modeling and analysis of a dissipative EMM for application in broadband wave attenuation at subwavelength scale. Wave dispersion behaviors of both non-dissipative and dissipative lattice systems with multiple resonators are studied to quantitatively determine microstructure effects on the form of a desired wave attenuation range. To reveal the working mechanisms, the dissipative EMM is homogenized as an

effective medium with an effective mass and an effective metadamping coefficient, from which wave attenuation can be quantitatively interpreted by both the negative effective mass density and effective metadamping. Finally, a microstructure design of the dissipative EMM made of the heterogeneous dissipative continuum media is numerically introduced as a potential EMM candidate for broadband wave attenuation. Hopefully, the results of the study could open new opportunities on the development of the new multifunctional composite material as an efficient wave mitigation material.

Acknowledgment

This work was supported by the Air Force Office of Scientific Research under Grant No. AF 9550-15-1-0061 with Program Manager Dr. Byung-Lip (Les) Lee.

References

[1] Pendry JB. Negative refraction makes a perfect lens. Phys Rev Lett 2000;85:3966–9.
[2] Tanaka T, Ishikawa A, Kawata S. Unattenuated light transmission through the interface between two materials with different indices of refraction using magnetic metamaterials. Phys Rev B 2006;73:125423.
[3] Cai W, Shalaev V. Optical metamaterials: fundamentals and applications. New York (USA): Springer; 2010.
[4] Li J, Chan CT. Double-negative acoustic metamaterial. Phys Rev E 2004;70:055602(R).
[5] Fang N, Lee H, Sun C, Zhang X. Sub-diffraction-limited optical imaging with a silver superlens. Science 2005;308:534–7.
[6] Yang Z, Mei J, Yang M, Chan NH, Sheng P. Membrane-type acoustic metamaterial with negative dynamic mass. Phys Rev Lett 2008;101:204301.
[7] Mei J, Ma GC, Yang M, Yang Z, Wen WJ, Sheng P. Dark acoustic metamaterials as super absorbers for low-frequency sound. Nat Commun 2012;3:756.
[8] Chen YY, Huang GL, Zhou XM, Hu GK, Sun CT. Analytical coupled vibroacoustic modeling of membrane-type acoustic metamaterials: membrane model. J Acoust Soc Am 2014;136:969–79.
[9] Chen YY, Huang GL, Zhou XM, Hu GK, Sun CT. Analytical coupled vibroacoustic modeling of membrane-type acoustic metamaterials: plate model. J Acoust Soc Am 2014;136:2926–34.
[10] Liu Z, Zhang X, Mao Y, Zhu YY, Yang Z, Chan CT, et al. Locally resonant sonic materials. Science 2000;289:1734–6.
[11] Yao SS, Zhou XM, Hu GK. Experimental study on negative effective mass in a 1D mass-spring system. New J Phys 2008;10:043020.
[12] Huang HH, Sun CT, Huang GL. On the negative mass density in acoustic metamaterials. Int J Eng Sci 2009;47:610–7.
[13] Lai Y, Wu Y, Sheng P, Zhang Z. Hybrid elastic solids. Nat Mater 2011;10:620–4.
[14] Liu XN, Hu GK, Huang GL, Sun CT. An elastic metamaterial with simultaneously negative mass density and bulk modulus. Appl Phys Lett 2011;98:251907.
[15] Zhu R, Liu XN, Hu GK, Sun CT, Huang GL. Negative refraction of elastic waves at the deep subwavelength scale in a single-phase metamaterial. Nat Commun 2014;5:5510.
[16] Huang GL, Sun CT. Band gaps in a multiresonator acoustic metamaterial. J Vib Acoust 2010;132:031003.
[17] Tan KT, Huang HH, Sun CT. Blast-wave impact mitigation using negative effective mass density concept of elastic metamaterials. Int J Impact Eng 2014;64:20–9.
[18] Zhu R, Liu XN, Hu GK, Sun CT, Huang GL. A chiral elastic metamaterial beam for broadband vibration suppression. J Sound Vib 2014;333:2759–73.
[19] Hussein MI, Frazier MJ. Metadamping: an emergent phenomenon in dissipative metamaterials. J Sound Vib 2013;332:4767–74.
[20] Manimala JM, Sun CT. Microstructural design studies for locally dissipative acoustic metamaterials. J Appl Phys 2014;135:023518.
[21] Pai PF, Peng H, Jiang S. Acoustic metamaterial beams based on multi-frequency vibration absorbers. Int J Mech Sci 2014;79:195–205.
[22] Del Prete E, Chinnayya A, Domergue L, Hadjadj A, Haas J-F. Blast wave mitigation by dry aqueous foams. Shock Waves 2013;23:39–53.
[23] Su Z, Peng W, Zhang Z, Gogos G, Skaggs R, Cheeseman B. Numerical simulation of a novel blast wave mitigation device. Int J Impact Eng 2007;35:336–46.
[24] Su Z, Peng W, Zhang Z, Gogos G, Skaggs R, Cheeseman B, et al. Experimental investigation of a novel blast wave mitigation device. Shock Vib 2009;16:543–53.
[25] Chen Y, Huang W, Constantini S. Blast shock wave mitigation using the hydraulic energy redirection and release technology. PLoS ONE 2012;7:e39353.
[26] Collet M, Ouisse M, Ruzzene M, Ichchouc MN. Floquet–Bloch decomposition for the computation of dispersion of two-dimensional periodic, damped mechanical systems. Int J Solids Struct 2011;48:2837–48.